Chemical Functional Groups Regulate Ion Concentrations and pHs in Nanopores

Yaguang Zhu[1], Prashant Gupta[2], Hamed Gholami Derami[2], Yin-Yuan Huang, Srikanth Singamaneni[2, *] and Young-Shin Jun[1, *]

[1]*Department of Energy, Environmental and Chemical Engineering, Washington University in St. Louis, St. Louis, Missouri, 63130, USA. E-mail: ysjun@seas.wustl.edu*

[2]*Department of Mechanical Engineering and Materials Science, Washington University in St. Louis, St. Louis, Missouri, 63130, USA. E-mail: singamaneni@wustl.edu*

Submitted: September 2024

Revised: December 2024

ACS Applied Materials & Interfaces

*To Whom Correspondence Should be Addressed

ABSTRACT

Understanding ion behaviors in functionalized nanopores is essential to deciphering reactions in both natural and engineered systems, such as sediments, biological ion channels, and membranes. While many efforts have shown the modified ion behaviors in the functionalized nanopores, a direct measurement and analysis to show how chemical functional groups affect ion concentrations in nanopores are critically needed. Herein, we present a synthesized plasmonic nanosensor that can measure the local concentrations of protons, anions (phosphate, nitrate, sulfate, and arsenate), and cations (mercury, lead, and copper) in functionalized nanopores, and we compare their concentrations in nanopores with the corresponding bulk concentrations. Notably, chemical functional groups induced ion concentrations differently in nanopores. In pristine nanopores and methyl- and phenyl-functionalized nanopores, we discovered an unexpected concurrence of an enhanced anion concentration and a suppressed cation concentration. In addition, the nanopore pH is dependent on bulk solution compositions and can be lower by 2.5 units, even when the bulk solution is well-buffered. In contrast, for hydrophilic (amine, thiol, and carboxyl) nanopores, pH depended on the pK_a of the functional groups, and the heavy metal concentrations depended on chemical interactions with the functional groups. Our findings can provide a better understanding of water chemistry in nanopores and can help precisely control ions in nanopores to benefit the design of membrane-based desalination techniques, CO_2 storage, and porous catalysts.

Keywords:

Nanopore, nanoconfinement, functional group, pH, ion behaviors

1. INTRODUCTION

Nanoporous structures can control the distribution and movement of ions and molecules in many natural and engineered systems.[1-7] For example, understanding how nanoporous sediments regulate gas flow is fundamental in evaluating shale gas deposits and optimizing their extraction.[1, 2] Moreover, ion-selective channels or nanopores in biological ion channels and nanoporous membranes can determine the selectivity of ion separations.[3-6] Therefore, elucidating ion−nanopore interactions tells us how the target species are precisely and selectively controlled. Understanding the contributions of functional groups on the nanopore surface is key to achieving a high level of control of ions in nanopore solutions. For example, biological ion channels with designed protein sequences and functionalized porous aromatic frameworks can capture and conduct specific ions through interactions between those ions and amine, carboxyl, or thiol groups.[8-10] In addition, the methyl groups and aromatic rings in sedimentary kerogen and hyper-crosslinked porous polymers can actively regulate the occurrence of organic compounds, such as hydrocarbon and plastic degradation products, respectively.[11, 12] These examples illustrate that deciphering how functional groups change ion behaviors in nanopore solutions can provide numerous beneficial insights.

Considering the significant roles of ion-pore interactions in the reactivity and utility of nanopores, numerous studies have investigated the effects of hydrophilic and hydrophobic nanopores on ion behaviors. For instance, overlapping hydrogen-bonding networks in a 2 nm hydrophilic nanochannel have been shown to enhance proton mobility.[13] Similarly, a hydrophobic sub 1 nm carbon nanotube has been reported to increase proton mobility by enhancing Grotthuss proton hopping.[14] Furthermore, ion mobility in hydrophilic nanopores is enhanced at low ion concentrations due to well-organized water structures but is reduced at high ion concentrations due

to the pairing and collisions of ions.[13, 15] Improved nanofluidic fabrication enabled us to identify how electrostatic interactions and steric effects control ion behaviors in geometrically and electrochemically confined systems[16-18]. Interestingly, The apparent pK_a inside the nanochannel differs from that in the solution[19], thereby tuning the ionic conductivities through modified acid−base equilibrium.[20] However, while previous studies have primarily focused on ion transport behaviors through nanopores, the relationship between ion concentrations in nanopore solutions and those in the bulk solution at equilibrium remains less explored. Understanding this relationship is crucial, especially in environmental applications. For example, assessing the distribution of toxic ions, such as Hg^{2+}, Pb^{2+}, and Cd^{2+}, between nanopore solutions and the bulk can provide insights into the fate and transport of these ions in soils and sediments. Currently, technologies allow sampling and measuring their ion concentrations only in the bulk solution.[21, 22] As another example, recently, nanoporous catalysts have garnered attention for their superior performance.[23, 24] Acquiring local concentrations of precursor ions in differently functionalized nanopores can enhance the understanding of catalytic reactions in the nanoporous catalysts, enabling more precise control in pore engineering.

In nanopores, ion concentrations can be affected by different physicochemical factors. Studies of ion transport in nanopores have found that electrostatic interactions can control the ion concentrations in nanopores.[25, 26] However, our recent work and that of Luo et al. (2015) have separately revealed that ion polarization can create specific physical interactions between ions and surfaces.[27, 28] We found that these interactions can dominate over electrostatic interactions in determining the ion concentrations in unfunctionalized silica nanopores,[28] and Luo et al. (2015) found the same dominance in carbon nanopores.[27] Importantly, because functional groups can chemically interact with ions, it remains unclear whether these physical interactions dominate ion

behaviors in functionalized nanopores. Yamaguchi et al. (2011) found that an amine group maintained the pH in nanopores when the bulk solution pH changed from 2 to 12. [29] Hence, to fully elucidate the interactions controlling ion behaviors in differently functionalized nanopores, *in situ,* highly sensitive, and localized measurements are needed because conventional methods using infrared and fluorescence scattering cannot differentiate the molecular signals from the bulk solution and the nanopore solution.

Here, we report a systematic study of ion concentrations in functionalized nanopores that leverages *in situ* surface-enhanced Raman spectroscopy (SERS) and an elaborately designed gold nanorod (AuNR) with a functionalized mesoporous silica ($mSiO_2$) core-shell plasmonic nanosensor. SERS takes advantage of a unique optical phenomenon called localized surface plasmon resonance (LSPR), which enhances electromagnetic fields within 10 nm of a nanoparticle surface by orders of magnitude (10^{10} to 10^{11}).[30, 31] This distance-dependent mechanism guaranteed that the pH and ion concentrations we obtained were from nanopores close to the AuNR surface. In this work, we focus on the pH and ion concentrations in functionalized nanopores at equilibrium with bulk solutions. Interestingly, entirely different pH and ion behaviors were observed when we used $mSiO_2$ shells functionalized with methyl, phenyl, carboxyl, amine, and thiol groups. Compared to the bulk solution concentrations, we found enhanced anion concentrations and suppressed cation concentrations in pristine and hydrophobic nanopores, meanwhile, the pH in these nanopores was highly dependent on the ionic strength of the bulk solution. In contrast, in hydrophilic nanopores, the pH and heavy metal concentrations were dependent on the specific chemical functional groups, and they changed little when the bulk solution concentration changed. Our newly discovered relationship between nanopore ion concentrations and bulk solutions has

significant implications for applications that exploit ions under confinement, such as catalysis, environmental remediation, and energy storage.

2. MATERIALS AND METHODS

2.1 Chemicals and Materials. This study used deionized (DI) water (≥ 18.2 MΩ·cm) obtained from a Barnstead Ultrapure Water System (D11931, Thermo Fisher Scientific) and American Chemical Society grade chemicals. Cetyltrimethylammonium bromide (CTAB), chloroauric acid ($HAuCl_4$), ortho-mercaptonicotinic acid (o-MNA), para-mercaptobenzoic acid (p-MBA), glycidol, ascorbic acid, tetraethyl orthosilicate (TEOS), ammonium hydroxide (NH_4OH), ammonium nitrate (NH_4NO_3), sodium borohydride ($NaBH_4$), sodium hydroxide (NaOH), L-ascorbic acid, silver nitrate ($AgNO_3$), (3-aminopropyl)triethoxysilane (APTES), (3-mercaptopropyl)triethoxysilane (MPTES), (3-cyanopropyl)triethoxysilane (CPTES), triethoxyphenylsilane (TEPhS), trimethoxy(propyl)silane (TMPS), mercury(II) chloride ($HgCl_2$), lead(II) chloride ($PbCl_2$), and copper(II) chloride ($CuCl_2$) were purchased from Sigma-Aldrich. Ethanol, sodium chloride (NaCl), dibasic sodium phosphate (Na_2HPO_4), sodium dihydrogen phosphate (NaH_2PO_4), and hydrochloric acid (HCl, 36.5–38.0%) were purchased from VWR International. All the chemicals were used as received, with no further purification. Milk substitute (Coffee Compliment®) tracer particles for surface zeta potential measurements were obtained from Premier International Foods (Spalding, UK) in pre-dispersed form. Silicon wafer (diam100mm/Type P/Dopant B/ Orien <100>/Res 10-20 ohm-cm/thick 500 um/ SSP prime) was procured from University Wafer.

2.2 Fabrication of Plasmonic Nanosensors. AuNRs functionalized with probe molecules (p-MBA@AuNR and o-MNA@AuNR) and m-SiO_2 coated functionalized AuNRs ($mSiO_2$@p-MBA@AuNR and $mSiO_2$@o-MNA@AuNR) were synthesized following our previously reported work (Figure 1a, see details in S1 in the Supporting Information).[28] The as-prepared $mSiO_2$@p-

MBA@AuNR and $mSiO_2$@o-MNA@AuNR nanosensors were termed "pristine" and further utilized for the fabrication of functionalized nanopores to investigate the effect of various functional groups on the pH and ion behaviors in nanopores. Taking advantage of the SiO_2 composition of the nanopore material, we utilized various organofunctional alkoxysilane molecules to generate functionalized nanopores via silanization. Briefly, 4.5 ml of $mSiO_2$@p-MBA@AuNR (extinction = 4) in ethanol was mixed with 0.25 ml of water, followed by addition of 0.25 ml APTES for generating amine functionalized nanopores. The above mixture was then stirred for 2 hours at room temperature. The as-prepared amine functionalized $mSiO_2$@p-MBA@AuNR nanoparticles were washed with ethanol and DI water 3 times each via centrifugation at 9000 rpm for 10 mins and finally redispersed in DI water for further use. Similarly, MPTES, CPTES, TEPhS, and TMPS were utilized to prepare thiol-, nitrile-, phenyl-, and methyl-functionalized $mSiO_2$@p-MBA@AuNR plasmonic nanosensors, respectively. The nitrile-functionalized $mSiO_2$@p-MBA@AuNR nanoparticles were further immersed in 1M HCl at 60^oC for 1 hour to obtain carboxyl functionalized $mSiO_2$@p-MBA@AuNR plasmonic nanosensors via hydrolysis of the nitrile functional group. The carboxyl-functionalized $mSiO_2$@p-MBA@AuNR nanoparticles were then washed with DI water 3 times and redispersed in DI water for further use. A similar procedure was employed to synthesize the other six functionalized $mSiO_2$@o-MNA@AuNR plasmonic nanosensors.

2.3 Characterization of Nanosensors. Transmission electron microscopy (TEM) images were obtained using a JEM-2100F (JEOL) field emission STEM at an operating voltage of 200 kV. UV–vis extinction spectra were obtained using a Shimadzu UV-1800 spectrophotometer. Zeta potential data were measured using a Malvern Zetasizer (Malvern ZEN3600). For characterizing the pore size and functional groups of the particles, pristine and functionalized mesoporous silica

coated AuNRs were freeze-dried overnight (LABCONCO FreeZone 4.5 Liter -84C Benchtop Freeze Dryer). The pore sizes of particles were measured by determining nitrogen adsorption isotherms through a pore size analyzer (Quantachrome Nova 2000e) at -196 °C through the BET protocol. Before the measurement, the powder samples (~0.3 g) were evacuated to a pressure of 10^{-4} Pa at 50 °C for 24 hours. Due to the huge amounts of nanosensors needed for this measurement, we only chose pristine and amine-functionalized nanosensors to study their pore characteristics. Pore size distributions were calculated using the Barrett–Joyner–Halenda protocol. The identities of the functional groups of the particles were confirmed by attenuated total reflection – Fourier transform infrared spectroscopy (Thermo Scientific Nicolet iS10 spectrometer).

2.4 Surface-Enhanced Raman Spectroscopy Measurement. SERS spectra were collected via a Renishaw inVia confocal Raman spectrometer using a 785 nm laser excitation wavelength (0.5 mW), which was focused using a 50× objective (NA = 0.9) with a 10 s exposure time. p-MBA@AuNR and o-MNA@AuNR were the nanosensors for measuring pH and ion concentrations in the bulk solutions, which can be considered as calibration experiments. Pristine and functionalized $mSiO_2$@p-MBA@AuNR and $mSiO_2$@o-MNA@AuNR were the nanosensors for measuring pH and ion concentrations in nanopore solutions.

For pH measurement, 50 mM phosphate buffer with and without the addition of 1 M NaCl was prepared in the pH range of 4–10. For pH measurement of bulk solutions, p-MBA@AuNRs were dispersed in different buffer solutions and their SERS spectra were measured. Plots showing the relationship between I_{1410}/I_{1080} from the p-MBA probe molecule and the local pH were obtained by analyzing these SERS spectra. All the calibration curves showed a typical sigmoidal shape, and they were fitted by the sigmoidal-Boltzmann equation, which has been successfully used in previous reports for fitting sigmoidal pH curves when using p-MBA to detect pH.[32, 33] Next,

pristine and functionalized $mSiO_2$@p-MBA@AuNR were dispersed in different buffer solutions. I_{1410}/I_{1080} values from the p-MBA probe molecule were obtained from the SERS spectra, and then these values were used for calculating the local pH in nanopores (pH_{pore}) by the calibration curve.

For anion measurement, 1 M Na_2HPO_4, NaH_2PO_4, $NaNO_3$, Na_2SO_4, and Na_3AsO_4 were used. p-MBA@AuNRs were dispersed in the solutions to obtain the SERS spectra, showing the intensity from anions in bulk solutions and p-MBA molecules. Meanwhile, pristine and functionalized $mSiO_2$@p-MBA@AuNRs were dispersed in solutions to obtain the SERS spectra showing the intensity from anions in nanopore solutions and p-MBA molecules. By using the intensities from p-MBA as internal standards, we could compare the anion concentrations between nanopore and bulk solutions.

For cation measurements, both 10 μM and 10 mM $HgCl_2$, $PbCl_2$, and $CuCl_2$ were used. Nanosensor o-MNA@AuNRs were dispersed in the solutions to obtain the SERS spectra showing the intensity from cations in bulk solutions. Meanwhile, pristine and functionalized $mSiO_2$@o-MNA@AuNRs were dispersed in solutions to obtain the SERS spectra showing the intensity from cations in nanopore solutions.

2.5 Determination of Functional Groups' pKa. A silicon wafer was employed to mimic the functionalization of the nanopore surface. The silicon substrate was cleaned with piranha solution (3:1 V/V mixture of H_2SO_4 and 30% H_2O_2), followed by treatment with APTES solution (4.5 ml ethanol, .25 ml DI water and 0.25 ml APTES) for 2 h. Next, the substrates were immersed in ethanol for 30 min, followed by ultrasonication for 10 min and thorough rinsing with ethanol and DI water to remove any excess and unbound APTES molecules. Finally, they were dried under a stream of nitrogen to realize amine-functionalized silicon substrates. Similarly, MPTES and CPTES were utilized to obtain thiol- and nitrile-functionalized silicon substrates. The carboxyl-

functionalized silicon substrate was obtained by treating nitrile-functionalized silicon substrate with 1M HCl at 60°C for 1 hour, followed by rinsing with DI water and subsequent drying under a stream of nitrogen. Then, we tracked the change of the surface zeta potential of prepared substrates at various pH to find the pK_a values of the functional groups. The surface zeta potential of the substrate surface was evaluated by a Malvern Zetasizer (Malvern ZEN3600) equipped with surface zeta potential cell (ZEN1020), as reported previously[34]. Measurements were performed with solutions containing 50 mM phosphate buffer (pH 2–12) and 1 mg/L of milk substitute tracer particles. After the measurements, surface zeta potential vs. pH plots were obtained for different functional groups (Figure S14). Because the pK_a values indicated that half of the functional groups were deprotonated, the corresponding surface zeta potential was the average value of the maximum and minimum of the surface zeta potential within the pH range. Therefore, we could determine the pK_a values of functional groups.

2.6 Monitoring pH change during glycidol rupture reaction. Solutions containing 750 mM NaCl and 150 mM glycidol were prepared, and the pH values were tuned to 3 by HCl. p-MBA@AuNR, pristine $mSiO_2$@p-MBA@AuNR, and carboxyl-functionalized $mSiO_2$@p-MBA@AuNR nanosensors were dispersed in the solutions. SERS spectra were collected to track the local pH changes. Meanwhile, the evolution of the bulk solution pH was also monitored by a VWR pH electrode, Model 89231-580 (Figure S13).

3. RESULTS AND DISCUSSION

3.1 Synthesis of nanosensors for detecting pH and ion behavior in functionalized nanopores. We synthesized AuNR and $mSiO_2$ coated AuNRs ($mSiO_2$@AuNR, includes both $mSiO_2$@p-MBA@AuNR and $mSiO_2$@o-MNA@AuNR, pristine) as nanosensors for detecting pH and ion behavior in the bulk solution and nanopore solution, respectively (Figure 1a; for details, see

Methods). AuNRs, with a well-controlled size and aspect ratio (Figure S1), are a SERS substrate that provides highly localized information about molecules within 10 nm of the AuNR surface.[30, 31] For $mSiO_2$@AuNR, only those ions and water molecules that can pass through the pores in the approximately 30 nm thick $mSiO_2$ layer and reach within 10 nm of the AuNR surface can be detected (Figure 3a). Chemical reactions between the silanol group and different precursors were utilized to achieve methyl, phenyl, carboxyl, amine, and thiol functionalization (Figure 1b; for details, see Materials and Methods). The functionalization did not significantly affect the characteristic transverse and longitudinal plasmon resonance bands in the extinction spectrum of AuNRs (Figure 3b, Figure S3c) or the porous structure of the mesoporous silica layer (Figure S4). To be noted, the aggregation of amine-functionalized nanosensors causes a small shift in their plasmon resonance band (Figure 3b and Figure S3c), but their porous structure is not changed (Figure S2 and S4). The red shift of plasmon resonance is not owing to the presence or thickness of mesoporous silica layer; all the other functionalized nanosensors have a mesoporous silica layer with a measured thickness 32 ± 5 nm (Figure S4), regardless of nanosensor functional groups. Because the TEM images do not have the quality to provide the pore size distribution, pore characteristics of the samples were studied from nitrogen adsorption/desorption isotherms. The pore size distribution was calculated using the Barrett–Joyner–Halenda protocol. The nanoprobes of $mSiO_2$@AuNR showed a broad pore size distribution ranging from 2–6 nm. The major two peaks of 2.6 nm, and 3.7 nm showed the bimodal pore size distribution in the nanosensor (Figure S2). After amine functionalization, we found that there is only one peak in the pore size distribution at 2.6 nm. In comparison with measurements from pristine nanopores, the different zeta potentials (Figure 3c) and peaks in the ATR-FTIR spectra (Figure 3d, Figure S5) near 1560 cm^{-1} (N-H bending)[35], 1590 cm^{-1} (COO^- stretching)[36], 680 cm^{-1} (C-S stretching)[37], 2970 cm^{-1} (C-H

stretching)[38], and 1480 cm^{-1} (C-C stretching in benzene ring)[35] confirmed the successful chemical functionalization.

AuNRs and mesoporous silica-coated AuNRs were used to measure the pH and ion concentrations in bulk solutions and nanopore solutions (Figure S6), respectively. Para-mercaptobenzoic acid (p-MBA) was used to detect the local pH. In the SERS spectra of p-MBA, the ratio of the peak intensity at the 1410 cm^{-1} Raman shift (COO^- stretching, which is pH sensitive) to the peak intensity at 1080 cm^{-1} (corresponding to benzene ring breathing and axial deformation that is pH insensitive) indicated the local pH change (Figure 2a). We first obtained the calibration curve describing the relationship between the peak intensity ratios (1410 cm^{-1}/1080 cm^{-1}) and local pH by dispersing p-MBA@AuNR in buffered solutions with known pH values (pH_{bulk}) (Figure S7). Then we dispersed pristine and functionalized mSiO_2@p-MBA@AuNR into buffered solutions and obtained the peak intensity ratios to calculate the pH in the nanopores (pH_{pore}), using the calibration curves. By using dispersed mesoporous silica coated nanosensors in different buffered solutions, we obtained the relationship between pH_{bulk} and pH_{pore}. When we changed the water chemistry in the bulk solution, we made a new calibration curve (Figure S7).

We also used plasmonic nanosensors to detect the cation and anion concentrations in nanopores. As mentioned above, AuNRs and mesoporous silica coated AuNRs respectively detect ions in the bulk and nanopores. Here, we first present the principle for measuring local anion concentrations. Due to the strong covalent bonding between p-MBA and AuNR, the intensities of Raman peak from p-MBA (e.g., peak at 1080 and 1590 cm^{-1}) have a minimum change after the mesoporous silica coating and further functionalization (Figure S8). Meanwhile, different anions have Raman scattering peaks at specific locations, and their local concentrations are proportional to the peak intensities. Therefore, we can use the peak intensities from p-MBA at 1080 cm^{-1} as an

internal standard in comparing the local concentrations of anions in the bulk and in nanopores (Figure 2b). Using this principle, our work successfully conducted measurements on phosphate ($H_2PO_4^-$ and HPO_4^{2-}), nitrate (NO_3^-), sulfate (SO_4^{2-}), and arsenate (AsO_4^{3-}) at a comparatively high 1 M concentration. The substantial spontaneous Raman scattering owing to the high concentrations will contribute to the Raman intensity in our measurements involving both AuNRs (which measure bulk concentrations) and functionalized $mSiO_2$@AuNRs (which measure nanopore concentrations). In addition, our anion concentration measurement is based on a ratiometric method that considers peaks from the anion of interest and an internal standard. Thus, the spontaneous Raman scattering would not change our comparison between the bulk and nanopore concentrations.

Next, considering cations, we chose to use ortho-mercaptonicotinic acid (o-MNA) as a probe molecule to detect three representative cations: mercury (Hg^{2+}), lead (Pb^{2+}), and copper (Cu^{2+}). With increasing local concentrations of these heavy metal cations, the intensity ratio between the two Raman peaks at 820 cm^{-1} and 860 cm^{-1} (I_{820}/I_{860}) decreased owing to the interactions between the carboxylic group in o-MNA and heavy metals,[39, 40] as illustrated in Figure 2c. The Raman peak at 820 cm^{-1} comes from the coupling vibration of O-H bending and pyridine ring deformation, and the Raman peak at 860 cm^{-1} corresponds to the coupling vibration of C-H bending and pyridine ring deformation.[39, 40] To stay within the detection range of o-MNA,[39] we measured local cation concentrations at 100 μM and 10 mM. The UV-Vis spectra for o-MNA@AuNR, pristine, and functionalized $mSiO_2$@o-MNA@AuNR are shown in Figure S3. In short, with our newly developed plasmonic nanosensors, we could determine the relationship between the ion concentrations in the bulk and nanopore solutions. Importantly, for all the cations and anions tested in this study, we individually measured their concentrations and did not study a

mixed salt system. In addition, as mentioned earlier, our local pH and ion concentration measurements were based on ratiometric methods from Raman peak intensities at fixed Raman shifts. This technique helps us to avoid interference from background intensities and guarantees obtaining accurate local concentrations, even when the local probe molecule amount is low. Even at low total Raman intensities, we can obtain the ratio of the Raman peak intensities, and these intensities are related only to the targeted ions and are not affected by other background ions.

To summarize, we used p-MBA as a SERS nanoprobe to detect local pH, used p-MBA as an internal standard to detect anions, and used o-MNA to detect heavy metals. It is important to note that the SERS enhancement is primarily confined within a short distance (~5–10 nm) near the plasmonic nanoparticle surfaces.[30, 31] Because the p-MBA@AuNR and o-MNA@AuNR nanosensors are in direct contact with the bulk solution, it can readily detect the aqueous chemistry there. As for the $mSiO_2$@p-MBA@AuNR and $mSiO_2$@o-MNA@AuNR nanosensors, because the $mSiO_2$ layer is thicker than 10 nm, it detected solution that had penetrated the nanoporous silica structure and traveled close to the AuNR surface. In our measurement, the nanopores consist of the spaces between the surface of the AuNR and the surface of the $mSiO_2$ and the nanopore spaces of $mSiO_2$ close to the AuNR (Figure S6b). The pH and ion concentration determination are in the nanoconfined space.

3.2 Pristine and hydrophobic nanopores: Opposite anion and cation behaviors, and the relation with pH in nanopores. As Figure 4a-c shows, the pH_{pore} behaviors in hydrophobic nanopores are similar to that in a pristine silica nanopore, and they all exhibit a dependence on the bulk solution compositions. In detail, pH_{pore} is similar to pH_{bulk} in a 50 mM phosphate buffer, whereas pH_{pore} becomes smaller than pH_{bulk} in a 50 mM phosphate buffer with 1 M NaCl (Figure 4a). Several recent studies found that the high proton transport rate in hydrophobic nanopores,

such as in carbon nanotubes and metal-organic nanotubes, could be attributed to the unique structure of water under confinement.[14, 41, 42] However, because the pH_{pore} behaviors we observed were dependent on the bulk solution compositions, fast proton conduction, which should be an intrinsic property of hydrophobic nanopores, cannot explain our finding. In addition, the surface distribution and pK_a of the silanol/siloxane group have also been suggested to affect pH in silica nanopores.[43] This mechanism should always make pH_{pore} smaller than pH_{bulk}, regardless of the bulk solution's ionic strengths and the concentrations of buffers. However, we observed experimentally that pH_{pore} was close to pH_{bulk} when the bulk solution was 50 mM. Therefore, local silanol/siloxane properties cannot explain our findings. Moreover, in solutions with higher ionic strengths, pristine and hydrophobic nanopores cannot attract more protons and decrease pH by electrostatic interactions, because they are less negatively charged in solutions with higher ionic strengths (Figure S9). Thus, electrostatic interactions were not the dominant mechanism controlling pH in pristine and hydrophobic nanopores.

Given that the proton concentrations were orders of magnitude lower than the ion concentrations in our study, we further investigated whether the pH_{pore} behaviors resulted from the modified ion concentrations in pristine, methyl, and phenyl functionalized nanopores. With the p-MBA molecule as an internal standard, we compared the anion concentrations in the functionalized nanopores with their bulk concentrations. In sodium salt solutions, the tested anions, including nitrate (NO_3^-), sulfate (SO_4^{2-}), arsenate (AsO_4^{3-}), dihydrogen phosphate ($H_2PO_4^-$), and monohydrogen phosphate (HPO_4^{2-}), all exhibited enhanced concentrations in pristine and hydrophobic nanopores (Figure 4d-e and Figure S10). With o-MNA as the probe molecule, we compared the heavy metal concentrations in the bulk solution and their concentrations in pristine and hydrophobic nanopore solutions. As shown in Figure 4f, the I_{820}/I_{860} value for 10 mM Hg^{2+}

bulk solution is 0.24. In contrast, the I_{820}/I_{860} values in pristine and hydrophobic nanopores were more than 0.4, which indicated a lower local concentration than the bulk concentration (Figure 4f). We also observed decreased Pb^{2+} and Cu^{2+} concentrations in pristine and hydrophobic nanopores (Figure S11). Interestingly, cations and anions behaved differently in pristine and hydrophobic nanopores. Both pristine and hydrophobic silica surfaces were negatively charged in our experimental systems (Figure 3c). If the ionic concentrations are only governed by electrostatic interactions, then we should have seen similar ionic concentrations for all the negatively charged nanopores. However, methyl coated nanosensors, whose zeta potential is similar to pristine nanosensors, showed a different enhancement of anion concentrations. Therefore, other interactions must dominate the ion behaviors in nanopores.

Polarization force in nanopores can provide an explanation. Previously, the polarization force has been found to separate oppositely charged ions at air-water interfaces[44, 45] and hydrophobic surface-water interfaces.[46, 47] Specifically, anisotropic solvation of anions induced substantially favorable dipole-dipole interactions, compensating for the loss of ion-dipole interactions, and caused large and polarizable anions to have a higher affinity towards the interface than cations do.[48, 49] In our pristine and hydrophobic nanoporous interface systems, with their high surface-to-volume ratio, we expected that these ion-surface specific interactions would enhance anion concentrations and suppress cation concentrations.[27, 28] To demonstrate how dispersion force can overcome electrostatic force in the hydrophobic nanopores, we modified the Poisson-Boltzmann equation by adding a new term related to dispersion force, and then we studied the cation and anion concentrations in nanopores (see details in S2 and Figure S12). The results showed that in a negatively charged nanopore, dispersion force can overcome electrostatic interactions to both enhance anion concentrations while simultaneously suppressing cation

concentrations. These results were consistent with our findings in both pristine and hydrophobic silica nanopores. Supporting this observation, an NMR study by Luo et al. (2015) also revealed the coexistence of enhanced anions (e.g., Cl^-, NO_3^-) and suppressed Na^+ concentrations in carbon nanopores, whose composition is similar to that of methyl and phenyl groups.[27] The methyl group might also induce stronger polarization force and thus resulted in a significantly enhanced anion concentrations compared to pristine and phenyl nanosensors. Additionally, the observation of counterintuitive ion concentrations in the nanopore resembles the charge inversion phenomenon in many chemical and biological systems, in which a strongly charged particle binds many counterions that its net charge changes.[50]

Chaotropic anions disrupt the hydrogen bonding network between water molecules while kosmotropic anions contribute to the stability and structure of water–water interactions.[27] In the work by Luo et al. (2015) , the chaotropic anions and kosmotropic anions would behave differently in the nanopores.[27] As the polarization force also plays an important role in our experimental system, we calculated the intensity enhancement factor (the intensities of Raman peak of anions in nanopores divided by those in the bulk solution) and found that the value followed the rank of arsenate < phosphate < nitrate, suggesting that chaotropic anions would have a higher concentration in the pore. This observation is consistent with the rank of chaotropic properties of anions. Meanwhile, we found that the sulfate, which is a kosmotropic anion, exhibited a high intensity enhancement factor. The local chemistry, the orientation of molecules, and the sulfate's own Raman sensitivity need to be explored further. As our gas adsorption data shows that the pores are in the size range of 2–6 nm (Figure S2). We further use a modeling to evaluate how the concentrations of cation and anion change with the pore size. As Figure S12c shows, when the pore size is a few nanometers, there is an obvious difference between the cation and anion

concentrations. This indicates that the polarization force-induced ion concentration change mainly occurs in nanopores with sizes of a few nanometers.

Previous works focusing on ion transport behavior in the field of nanopore sensing/ion rectification have shown that manipulating surface functional group properties or changing surface charge by an external electric source on a single nanopore can control ion transport behavior in nanopores.[51, 52] However, in our study, we measured the average ion concentrations in many nanopores surrounding the AuNR, and thus any single nanopore's performance had a small impact on our results. Moreover, this study and other recent work[27, 53] highlight that electrostatic force is not always the only dominant driving force to govern ion concentrations in nanopores, especially when we consider both the nanopore and bulk solutions.

These modified ion concentrations in pristine and hydrophobic nanopores can help us to understand the pH_{pore} behavior. As a consequence of the opposite behaviors of cations and anions in nanopores, protons are needed to compensate for the excess of negative charges there and we could expect a smaller pH_{pore} than pH_{bulk}. However, our SERS results showed that pH_{pore} behaviors also depended on the compositions of the pH-buffered bulk solutions, a finding that indicates competition between the pH buffer and the excess negative charge in the nanopores. In our previous work[28], using numerical modeling, we compared the concentration differences between cations and anions in nanopores with different buffer capacities in pristine silica nanopores. At low solution concentrations (< 0.2 M), although electroneutrality breakdown occurred, the buffers provided sufficient protons because the ionic concentration differences (anion concentrations minus cation concentrations) were smaller than the buffer capacities. This result can explain why pH_{pore} was close to pH_{bulk} when we used 50 mM phosphate buffer. On the other hand, at high solution concentrations (> 0.2 M), the extremely high ionic concentration differences (i.e., anion

concentration - cation concentration) recruited great quantities of protons and overwhelmed the buffer capacities, so the pH_{pore} value was lower than pH_{bulk}, as seen in the case of 50 mM phosphate buffer with 1 M NaCl. In our current study, hydrophobic nanopores also induced opposite anion and cation behaviors, as a pristine silica nanopore does. Therefore, both pristine and hydrophobic nanopores exhibit much lower pH_{pore} at high solution concentration (Figure 4b-c) due to the mechanism mentioned above.

3.3 Hydrophilic nanopores: Chemical functional group-dependent pH and heavy metal concentrations. Building on our understanding of the pristine and the two hydrophobic nanopores, we examined new nanopores with hydrophilic functionalities: amine, thiol, and carboxyl groups. pH_{pore} in these hydrophilic functionalized nanopores showed several intriguing results (Figure 5a-c). First, pH_{pore} values in hydrophilic nanopores were independent of the ionic strengths of the bulk solutions, which was clearly different from the pH_{pore} behavior in pristine and hydrophobic nanopores. Second, pH_{pore} underwent small changes when pH_{bulk} changed from 4 to 10. Specifically, pH_{pore} fell in the ranges of 6.0–8.0, 5.6–7.1, and 4.0–7.7 for amine-, thiol-, and carboxyl-functionalized nanopores, respectively. Third, each hydrophilic functional group caused a distinctly different pH_{pore} behavior. These observations strongly suggested that hydrophilic functional groups in nanopores controlled pH through functional group-specific interactions, which are more powerful than the physical interactions we discovered in the pristine and hydrophobic nanopores.

To further validate that the surface chemistry governed the pH in carboxyl functionalized nanopores, we used our nanosensors to track pH change in bulk solutions, pristine nanopores, and carboxyl nanopores during a pH-changing chemical reaction (Figure 6). Prior to the experiments, zeta potential and FTIR observations confirmed that the nanosensors were successfully

functionalized with carboxyl groups. Homogeneous alkalization driven by chloride-assisted glycidol rupture (Figure 6a)[54, 55] quickly increased the pH of the bulk solution, from 3 to 10 within 30 minutes (Figure S13). For both p-MBA@AuNR and pristine $mSiO_2$@p-MBA@AuNR, we observed a peak intensity increase at 1410 cm^{-1} (I_{1410}/I_{1080} increases from 0.01 to more than 0.3, corresponding to a local pH increase from 3 to 9.5), consistent with a previous study showing this alkalization reaction in mesoporous titanium dioxide.[55] In contrast, there is only a small peak intensity increase at 1410 cm^{-1} for carboxyl functionalized $mSiO_2$@p-MBA@AuNR (I_{1410}/I_{1080} increases from 0.01 to more than 0.09, corresponding to a local pH increase from 3 to 6 (Figure 6b). This difference demonstrated that the carboxyl group in nanopores could maintain pH_{pore} at close to 6, even though the reaction generated large quantities of hydroxide. Using fluorescence measurement, Yamaguchi et al. (2011) reported that pH_{pore} in amine-functionalized silica nanopores increased by only 1.8 units when pH_{bulk} changed from 2.1 to 9.1, but the mechanism was not further explored.[29] Inspired by the strong correlation between proton transport and the acidity of functional groups on pore surfaces (COOH, $PO(OH)_2$, and SO_3H),[56] we hypothesized that pH_{pore} was dependent on the pK_a values of functional groups on the pore surfaces. To test this hypothesis, we evaluated the pK_a values of amine, carboxyl, and thiol groups by surface zeta potential measurements of functionalized silica substrates at varying pH values (see Materials and Methods). The results indicated pK_a values for amine, thiol, and carboxyl groups of around 7.5, 7, and 5, respectively (Figure S14). These values were close to the pK_a values for these functional groups measured by Fourier-transform infrared spectroscopy and chemical force microscopy.[57, 58] As previously mentioned, the pH values of the intersections between pH_{pore} and pH_{bulk} fall in the ranges of 7–8, 6–7, and 4–7 for amine-, thiol-, and carboxyl-functionalized nanopores, respectively. These values are close to the functional group pK_a values. The amine and thiol groups in nanopore

make the nanopore solution have neutral pH. In addition, the carboxyl group in the nanopore makes the nanopore solution become acidic. These values are close to the pK_a values of amine-, thiol-, and carboxyl groups. At the pK_a value of the functional group, the functional group would have the largest pH buffer capacity[59], which could explain the results.

In this study, these hydrophilic groups in nanopores also controlled the behaviors of heavy metals (Hg^{2+}, Pb^{2+}, and Cu^{2+}). For example, when o-MNA@AuNR was used to detect the bulk Hg^{2+}, the o-MNA complexed with Hg^{2+}. Without nanoconfinement, the I_{820}/I_{860} changed from 0.70 to 0.24 (Figure 5d) when the bulk Hg^{2+} concentration was increased from 100 μM to 10 mM. However, as Figure 5d and Figure S15 show, in nanopores, the spectra for hydrophilic functionalized $mSiO_2$@o-MNA@AuNR and the I_{820}/I_{860} values show only small changes when the bulk concentrations are increased from 100 μM to 10 mM. Specifically, as seen in Figure 5d, the I_{820}/I_{860} values change from 0.83 to 0.78 for thiol-functionalized nanopores, from 0.22 to 0.19 for amine-functionalized nanopores, and remain at 0.34 for carboxyl-functionalized nanopores. Moreover, comparing these values with the I_{820}/I_{860} values measured by o-MNA@AuNR, we found that each functional group caused a distinctively different heavy metal concentration in nanopores: < 100 μM in thiol-functionalized nanopores, > 10 mM in amine-functionalized nanopores, and 100 μM–10 mM in carboxyl-functionalized nanopores. These trends also occur in Pb^{2+} and Cu^{2+} systems.

Two possible mechanisms could explain these findings. First, when heavy metals enter nanopores, they can either complex with the hydrophilic functional groups or remain as free heavy metals in nanopore solutions ($C_{\text{total metal}} = C_{\text{metal complexed with functional groups}} + C_{\text{free metal}}$). The free heavy metal portion can complex with o-MNA probe molecules and be measured using SERS. These "free" heavy metals would be critical information in identifying the bioavailable and bioaccessible

metal ions in soils and sediments and connecting them with their harmful results. While our method provides new information about free metal ion concentrations in nanopores, it cannot measure the total heavy metal concentrations in the nanopores because of strong interactions between metal ions and functional groups and the unmeasurable functional group densities in nanopores. Developing new methods to measure total metal concentrations ($C_{total\ metal}$) and functional group densities in nanopores is an important future research direction.

Our work compared three functional groups and obtained the correlation between free heavy metal concentrations and the identity of amine/carboxyl/thiol groups. The comparison of heavy metal concentrations in nanopores indicates that different surface functional groups can have diverse interactions with heavy metals. For example, the thiol group can form complexes with mercury, as described in the hard/soft acid/base (HSAB) theory.[8] Thus, mercury tends to stay on the surface of a thiol-functionalized nanopore.

Second, both chemical and physical interactions can impact heavy metals. To further test whether the physical interactions we found in pristine and hydrophobic nanopores still existed in hydrophilic nanopores, we evaluated the anion behaviors in them. The enhanced anion concentrations in hydrophilic nanopores confirmed that physical interactions caused by ion polarization can still affect anion concentrations (Figure 5e-f and Figure S10). On the other hand, heavy metal cations in hydrophilic nanopores were affected by both chemical and physical interactions. In addition, even though there are unbalanced concentrations between cations and anions in hydrophilic nanopores, their impacts on pH are clearly less than the functional group's impacts (*i.e.,* pK_a) on the pH. Our results also show that the pH in hydrophilic nanopores is independent of the ionic strength of the bulk solution, which is clearly different from that of hydrophobic nanopores. Local pH is an important factor in controlling heavy metal concentrations

because it can alter the speciation of heavy metals and functional group protonation/deprotonation. In our study, we found that both thiol and amine groups can maintain the nanopore pH around neutral. However, these two groups caused significantly different heavy metal concentrations: thiol groups caused lower heavy metal concentrations, while the amine group caused higher heavy metal concentrations. Thus, we conclude that pH is not a dominant factor in controlling heavy metal concentrations in the nanopore.

Heavy metals and protons can complex differently with silanol groups and hydrophilic functional groups in the nanopores. Previous studies have discovered that hydrophilic functionalized mesoporous silica can extract more water (with microgravimetric measurements) and adsorb more mercury (with batch adsorption experiments) than pristine mesoporous silica[60, 61]. These previous work suggest that amine and carboxyl groups are more hydrophilic than silanol groups, but the detailed molecular mechanisms have not been studied. In our experiment, both the methyl and phenyl groups hardly have protonation or deprotonation reaction and thus they cannot achieve a pH buffering effects. For pristine mesoporous silica-coated AuNR, the silanol group might have a weaker interaction with protons compared to other hydrophilic groups. However, it is difficult to experimentally probe the functional group's interactions with protons in the nanopores. For example, the local surface heterogeneities can cause the pK_a values of silanol groups ranging from 2.3 to 10.7 along the wall of a single capillary[43]. Such measurements have not been done for amine, carboxyl, and thiol groups. Thus, there are many exciting future research opportunities that can develop new experimental tools to directly probe the chemical bond in the nanopores and work with modeling tools to understand the extinct complexation behaviors in the nanopores.

4. CONCLUSIONS

This study presents the first *in situ* measurements of solution ion concentrations in nanopores with variously functionalized surfaces. With our newly developed plasmonic nanosensors, we achieved highly localized measurements of protons, anions (phosphate, nitrate, sulfate, and arsenate), and cations (free mercury, lead, and copper) in both bulk solutions and nanopore solutions. Notably, we discovered that hydrophobic functional groups (methyl and phenyl) and hydrophilic functional groups (amine, carboxyl, and thiol) resulted in entirely different ion concentrations in nanopores. In hydrophobic functionalized nanopores, enhanced anion concentrations coincided with suppressed cation concentrations, possibly due to the polarizability difference between anions and cations. Further, owing to the concentration difference between anions and cations, large numbers of protons were required to compensate for the excess negative charge in the nanopore. This phenomenon resulted in a lower pH_{pore} than pH_{bulk} at high ionic strengths, even in a well-buffered system. In contrast, in the hydrophilic nanopores, the interactions between functional groups and ions were dominant. Specifically, amine and thiol groups can maintain the pH near neutral, while the carboxyl group results in an acidic pH in the nanopore, regardless of the ionic strength and pH in bulk solution. These chemical interactions drive the pH in nanopores towards the pK_a values of the functional groups. In addition, functional groups determine the heavy metal concentrations in the nanopore, regardless of the bulk concentrations.

The novel *in situ* technique of using SERS measurements of functionalized mesoporous silica-coated gold nanorods to obtain valuable nanopore information can be applied in multiple fields. Future work can develop novel SERS-based nanosensor to separately evaluate the nanopore chemistry at pores close to AuNR surface and the pores which are a few nanometers away from the AuNR surface. In addition, our work observed distinctly different concentrations of pollutants, *i.e.,* arsenate and heavy metals, in functionalized nanopore solutions and bulk solutions, which

could directly guide environmental remediation of sediments and soils. Understanding the mechanisms that control ion concentrations in confined spaces is also paramount in developing highly efficient catalysts and energy storage materials. Moreover, by elucidating the physical and chemical interactions, our work can help to achieve high local concentrations of anion precursors or cation precursors in nanoporous systems.

Mesoporous materials modified with functional groups have substantial impacts in various fields mentioned earlier. Future studies can coat different types of mesoporous materials on AuNRs, such as porous carbon and porous metal-organic framework, and study the aqueous chemistries in these nanopores. In addition, a systematic evaluation of the effect of pore size on pH and ion concentrations can provide further guidance for controlling reactivities and performances of different porous materials in aqueous environments. Our nanosensor design can be extended to include other mesoporous materials and probe molecules to provide more helpful information in the fields of biosensing and nanofluidics. We envision that these new designs and new findings will advance our fundamental understanding of ion behaviors under nanoconfinement.

Supporting Information

Experimental details; numerical modeling details; TEM image of synthesized AuNRs; Pore size distributions of pristine and amine-functionalized mSiO2@AuNR; Supporting UV-Vis spectra of the nanosensors; TEM images of nanosensors; Supporting FTIR spectra of pristine- and thiol-functionalized nanosensor; Schematics of the measurement of pH and ions in bulk solution and in nanopore solution; Calibration curves for ratios of peak intensities (I_{1410}/I_{1080}) with respect to pH_{bulk} in different buffers obtained from p-MBA@AuNR; Raman spectra of nanosensors in 50 mM phosphate buffer with 1 M NaCl solution at pH 5; Change in zeta potentials of nanosensors

with respect to the solution pH; SERS spectra of SO_4^{2-}, AsO_4^{3-}, and HPO_4^{2-} in bulk solutions and functionalized nanopore solutions; SERS measurement lead and copper in bulk, pristine nanopore , methyl-functionalized nanopore, and phenyl-functionalized nanopore solutions; Numerical modeling results; pH evolution in bulk solution during the glycidol rupture reaction; Change in surface zeta potentials of functionalized substrates with pH; SERS measurement lead and copper in bulk, amine-functionalized nanopore, thiol-functionalized nanopore, and carboxyl-functionalized nanopore solutions.

ACKNOWLEDGEMENTS

The project was supported by American Chemical Society's Petroleum Research Fund (62756-ND5) and the U.S. Department of Energy Office of Science (DE-SC0023390). S.S., P.G., and H.G.D. are supported by Air Force Office of Scientific Research (Award # FA95502310461) and the National Science Foundation (Award # 2331330). The Nano Research Facility and the Institute of Materials Science & Engineering at Washington University in St. Louis provided their facilities for the experiments. We thank Dr. Yunzhu Zhang for helping with the surface zeta potential measurements. We thank Prof. James Ballard for carefully reviewing the manuscript.

Competing interests

There are no conflicts to declare.

References

(1) Javadpour, F.; Fisher, D.; Unsworth, M. Nanoscale gas flow in shale gas sediments. *J. Can. Pet. Technol.* **2007**, *46* (10), 55-61.
(2) Tournassat, C.; Steefel, C. I. J. R. i. M.; Geochemistry. Reactive transport modeling of coupled processes in nanoporous media. *Rev. Mineral. Geochem.* **2019**, *85* (1), 75-109.
(3) Clapham, D. E.; Runnels, L. W.; Strübing, C. The TRP ion channel family. *Nat. Rev. Neurosci.* **2001**, *2* (6), 387.
(4) Gouaux, E.; MacKinnon, R. Principles of selective ion transport in channels and pumps. *Science* **2005**, *310* (5753), 1461-1465.
(5) Werber, J. R.; Osuji, C. O.; Elimelech, M. Materials for next-generation desalination and water purification membranes. *Nat. Rev. Mater.* **2016**, *1* (5), 1-15.
(6) Elimelech, M.; Phillip, W. A. The future of seawater desalination: energy, technology, and the environment. *Science* **2011**, *333* (6043), 712-717.
(7) Epsztein, R.; DuChanois, R. M.; Ritt, C. L.; Noy, A.; Elimelech, M. Towards single-species selectivity of membranes with subnanometre pores. *Nat. Nanotechnol.* **2020**, *15* (6), 426-436.
(8) Uliana, A. A.; Bui, N. T.; Kamcev, J.; Taylor, M. K.; Urban, J. J.; Long, J. R. Ion-capture electrodialysis using multifunctional adsorptive membranes. *Science* **2021**, *372* (6539), 296-299.
(9) Demir, S.; Brune, N. K.; Van Humbeck, J. F.; Mason, J. A.; Plakhova, T. V.; Wang, S.; Tian, G.; Minasian, S. G.; Tyliszczak, T.; Yaita, T. Extraction of lanthanide and actinide ions from aqueous mixtures using a carboxylic acid-functionalized porous aromatic framework. *ACS Cent. Sci.* **2016**, *2* (4), 253-265.
(10) Jasti, J.; Furukawa, H.; Gonzales, E. B.; Gouaux, E. Structure of acid-sensing ion channel 1 at 1.9 Å resolution and low pH. *Nature* **2007**, *449* (7160), 316-323.
(11) Bousige, C.; Ghimbeu, C. M.; Vix-Guterl, C.; Pomerantz, A. E.; Suleimenova, A.; Vaughan, G.; Garbarino, G.; Feygenson, M.; Wildgruber, C.; Ulm, F.-J. Realistic molecular model of kerogen's nanostructure. *Nat. Mater.* **2016**, *15* (5), 576-582.
(12) Chen, L.; Rong, M.; Yang, L.; Yu, J.; Qu, H.; Meng, Q.; Ni, S.; Xu, Z.; Zhu, X.; Wang, L. Construction of super-hydrophobic hypercrosslinked porous polymers for selectively removing aromatic diamines from the polyurethane bio-hydrolysate. *Chem. Eng. J.* **2022**, *428*, 132509.
(13) Duan, C.; Majumdar, A. Anomalous ion transport in 2-nm hydrophilic nanochannels. *Nat. Nanotechnol.* **2010**, *5* (12), 848.
(14) Tunuguntla, R. H.; Allen, F. I.; Kim, K.; Belliveau, A.; Noy, A. Ultrafast proton transport in sub-1-nm diameter carbon nanotube porins. *Nat. Nanotechnol.* **2016**, *11* (7), 639-644.
(15) Ma, J.; Li, K.; Li, Z.; Qiu, Y.; Si, W.; Ge, Y.; Sha, J.; Liu, L.; Xie, X.; Yi, H. Drastically reduced ion mobility in a nanopore due to enhanced pairing and collisions between dehydrated ions. *J. Am. Chem. Soc*. **2019**, *141* (10), 4264-4272.
(16) Daiguji, H. Ion transport in nanofluidic channels. *Chem. Soc. Rev.* **2010**, *39* (3), 901-911.
(17) Liu, P.; Kong, X.-Y.; Jiang, L.; Wen, L. Ion transport in nanofluidics under external fields. *Chem. Soc. Rev.* **2024**.
(18) Kim, S.; Choi, H.; Kim, B.; Lim, G.; Kim, T.; Lee, M.; Ra, H.; Yeom, J.; Kim, M.; Kim, E. Extreme Ion-Transport Inorganic 2D Membranes for Nanofluidic Applications. *Adv. Mater.* **2023**, *35* (43), 2206354.
(19) Tagliazucchi, M.; Azzaroni, O.; Szleifer, I. Responsive polymers end-tethered in solid-state nanochannels: when nanoconfinement really matters. *J. Am. Chem. Soc*. **2010**, *132* (35), 12404-12411.

(20) Tagliazucchi, M.; Rabin, Y.; Szleifer, I. Ion transport and molecular organization are coupled in polyelectrolyte-modified nanopores. *J. Am. Chem. Soc*. **2011**, *133* (44), 17753-17763.
(21) Liu, L.; Zhang, C.; Jiang, W.; Li, X.; Dai, Y.; Jia, H. Understanding the sorption behaviors of heavy metal ions in the interlayer and nanopore of montmorillonite: A molecular dynamics study. *J. Hazard. Mater.* **2021**, *416*, 125976.
(22) Gobeil, C.; Cossa, D. Mercury in sediments and sediment pore water in the Laurentian Trough. *Can. J. Fish. Aquat.* **1993**, *50* (8), 1794-1800.
(23) Pascanu, V.; González Miera, G.; Inge, A. K.; Martín-Matute, B. n. Metal–organic frameworks as catalysts for organic synthesis: a critical perspective. *J. Am. Chem. Soc*. **2019**, *141* (18), 7223-7234.
(24) Leenders, S. H.; Gramage-Doria, R.; de Bruin, B.; Reek, J. N. Transition metal catalysis in confined spaces. *Chem. Soc. Rev.* **2015**, *44* (2), 433-448.
(25) Kovaleva, E. G.; Molochnikov, L. S.; Tambasova, D.; Marek, A.; Chestnut, M.; Osipova, V. A.; Antonov, D. O.; Kirilyuk, I. A.; Smirnov, A. I. Electrostatic properties of inner nanopore surfaces of anodic aluminum oxide membranes upon high temperature annealing revealed by EPR of pH-sensitive spin probes and labels. *J. Membr. Sci.* **2020**, *604*, 118084.
(26) Kovaleva, E. G.; Molochnikov, L. S.; Venkatesan, U.; Marek, A.; Stepanova, D. P.; Kozhikhova, K. V.; Mironov, M. A.; Smirnov, A. I. Acid–base properties of nanoconfined volumes of anodic aluminum oxide pores by EPR of pH-sensitive spin probes. *J. Phys. Chem. C* **2016**, *120* (5), 2703-2711.
(27) Luo, Z.-X.; Xing, Y.-Z.; Ling, Y.-C.; Kleinhammes, A.; Wu, Y. Electroneutrality breakdown and specific ion effects in nanoconfined aqueous electrolytes observed by NMR. *Nat. Commun.* **2015**, *6*, 6358.
(28) Zhu, Y.; Derami, H. G.; Gupta, P.; Gupta, R.; Singamaneni, S.; Jun, Y.-S. Ionic surface propensity controls pH in nanopores. *Chem* **2022**, *8* (11), 3081-3095.
(29) Yamaguchi, A.; Namekawa, M.; Kamijo, T.; Itoh, T.; Teramae, N. Acid−base equilibria inside amine-functionalized mesoporous silica. *Anal. Chem.* **2011**, *83* (8), 2939-2946.
(30) Haes, A. J.; Haynes, C. L.; McFarland, A. D.; Schatz, G. C.; Van Duyne, R. P.; Zou, S. Plasmonic materials for surface-enhanced sensing and spectroscopy. *MRS Bull.* **2005**, *30* (5), 368-375.
(31) Reguera, J.; Langer, J.; de Aberasturi, D. J.; Liz-Marzán, L. M. Anisotropic metal nanoparticles for surface enhanced Raman scattering. *Chem. Soc. Rev.* **2017**, *46* (13), 3866-3885.
(32) Jamieson, L. E.; Jaworska, A.; Jiang, J.; Baranska, M.; Harrison, D.; Campbell, C. Simultaneous intracellular redox potential and pH measurements in live cells using SERS nanosensors. *Analyst* **2015**, *140* (7), 2330-2335.
(33) Wei, H.; Vejerano, E. P.; Leng, W.; Huang, Q.; Willner, M. R.; Marr, L. C.; Vikesland, P. J. Aerosol microdroplets exhibit a stable pH gradient. *Proc. Natl. Acad. Sci. U.S.A.* **2018**, *115* (28), 7272-7277.
(34) Corbett, J. C.; McNeil-Watson, F.; Jack, R. O.; Howarth, M. Measuring surface zeta potential using phase analysis light scattering in a simple dip cell arrangement. *Colloids Surf., A* **2012**, *396*, 169-176.
(35) Llusar, M.; Monrós, G.; Roux, C.; Pozzo, J. L.; Sanchez, C. One-pot synthesis of phenyl- and amine-functionalized silica fibers through the use of anthracenic and phenazinic organogelators. *J. Mater. Chem.* **2003**, *13* (10), 2505-2514.

(36) Papageorgiou, S. K.; Kouvelos, E. P.; Favvas, E. P.; Sapalidis, A. A.; Romanos, G. E.; Katsaros, F. K. Metal–carboxylate interactions in metal–alginate complexes studied with FTIR spectroscopy. *Carbohydr. Res.* **2010**, *345* (4), 469-473.
(37) Bastian Jr, E. J.; Martin, R. B. Disulfide vibrational spectra in the sulfur-sulfur and carbon-sulfur stretching region. *J. Phys. Chem.* **1973**, *77* (9), 1129-1133.
(38) Matei, C.; Buhălţeanu, L.; Berger, D.; Mitran, R.-A. Functionalized mesoporous silica as matrix for shape-stabilized phase change materials. *Int. J. Heat Mass Transfer* **2019**, *144*, 118699.
(39) Tan, E.; Yin, P.; Lang, X.; Zhang, H.; Guo, L. A novel surface-enhanced Raman scattering nanosensor for detecting multiple heavy metal ions based on 2-mercaptoisonicotinic acid functionalized gold nanoparticles. *Spectrochim. Acta, Part A* **2012**, *97*, 1007-1012.
(40) Karabacak, M.; Kurt, M. Comparison of experimental and density functional study on the molecular structure, infrared and Raman spectra and vibrational assignments of 6-chloronicotinic acid. *Spectrochim. Acta, Part A* **2008**, *71* (3), 876-883.
(41) Cao, Z.; Peng, Y.; Yan, T.; Li, S.; Li, A.; Voth, G. A. Mechanism of fast proton transport along one-dimensional water chains confined in carbon nanotubes. *J. Am. Chem. Soc*. **2010**, *132* (33), 11395-11397.
(42) Otake, K.-i.; Otsubo, K.; Komatsu, T.; Dekura, S.; Taylor, J. M.; Ikeda, R.; Sugimoto, K.; Fujiwara, A.; Chou, C.-P.; Sakti, A. W. Confined water-mediated high proton conduction in hydrophobic channel of a synthetic nanotube. *Nat. Commun.* **2020**, *11* (1), 1-7.
(43) Macias-Romero, C.; Nahalka, I.; Okur, H. I.; Roke, S. Optical imaging of surface chemistry and dynamics in confinement. *Science* **2017**, *357* (6353), 784-788.
(44) Ghosal, S.; Hemminger, J. C.; Bluhm, H.; Mun, B. S.; Hebenstreit, E. L.; Ketteler, G.; Ogletree, D. F.; Requejo, F. G.; Salmeron, M. Electron spectroscopy of aqueous solution interfaces reveals surface enhancement of halides. *Science* **2005**, *307* (5709), 563-566.
(45) Piatkowski, L.; Zhang, Z.; Backus, E. H.; Bakker, H. J.; Bonn, M. Extreme surface propensity of halide ions in water. *Nat. Commun.* **2014**, *5* (1), 1-7.
(46) Horinek, D.; Netz, R. R. Specific ion adsorption at hydrophobic solid surfaces. *Phys. Rev. Lett.* **2007**, *99* (22), 226104.
(47) Bauer, B. A.; Ou, S.; Patel, S. Role of spatial ionic distribution on the energetics of hydrophobic assembly and properties of the water/hydrophobe interface. *PCCP* **2012**, *14* (6), 1892-1906.
(48) Tobias, D. J.; Jungwirth, P.; Parrinello, M. Surface solvation of halogen anions in water clusters: an ab initio molecular dynamics study of the $Cl^-(H_2O)_6$ complex. *J. Chem. Phys.* **2001**, *114* (16), 7036-7044.
(49) Jungwirth, P.; Tobias, D. J. Molecular structure of salt solutions: a new view of the interface with implications for heterogeneous atmospheric chemistry. *J. Phys. Chem. B* **2001**, *105* (43), 10468-10472.
(50) Grosberg, A. Y.; Nguyen, T.; Shklovskii, B. Colloquium: The physics of charge inversion in chemical and biological systems. *Rev. Mod. Phys.* **2002**, *74* (2), 329.
(51) Wen, C.; Zeng, S.; Li, S.; Zhang, Z.; Zhang, S.-L. On rectification of ionic current in nanopores. *Anal. Chem.* **2019**, *91* (22), 14597-14604.
(52) Shi, W.; Friedman, A. K.; Baker, L. A. Nanopore sensing. *Anal. Chem.* **2017**, *89* (1), 157-188.
(53) Son, C. Y.; Wang, Z.-G. Image-charge effects on ion adsorption near aqueous interfaces. *Proc. Natl. Acad. Sci. U.S.A.* **2021**, *118* (19), e2020615118.

(54) Parker, R.-E.; Isaacs, N. Mechanisms of epoxide reactions. *Chem. Rev.* **1959**, *59* (4), 737-799.
(55) Zalduendo, M. M.; Oestreicher, V.; Langer, J.; Liz-Marzán, L. M.; Angelomé, P. C. Monitoring Chemical Reactions with SERS-Active Ag-Loaded Mesoporous TiO_2 Films. *Anal. Chem.* **2020**, *92* (20), 13656-13660.
(56) Bibent, N.; Mehdi, A.; Silly, G.; Henn, F.; Devautour-Vinot, S. Proton conductivity versus acidic strength of one-pot synthesized acidic functionalized SBA-15 Mesoporous silica. *Eur. J. Inorg. Chem.* **2011**, 3214-3225.
(57) Gershevitz, O.; Sukenik, C. N. *In situ* FTIR-ATR analysis and titration of carboxylic acid-terminated SAMs. *J. Am. Chem. Soc*. **2004**, *126* (2), 482-483.
(58) Vezenov, D. V.; Noy, A.; Rozsnyai, L. F.; Lieber, C. M. Force titrations and ionization state sensitive imaging of functional groups in aqueous solutions by chemical force microscopy. *J. Am. Chem. Soc*. **1997**, *119* (8), 2006-2015.
(59) Benjamin, M. M. *Water chemistry*; Waveland Press, 2014.
(60) Lee, B.; Kim, Y.; Lee, H.; Yi, J. Synthesis of functionalized porous silicas via templating method as heavy metal ion adsorbents: the introduction of surface hydrophilicity onto the surface of adsorbents. *Microporous Mesoporous Mater.* **2001**, *50* (1), 77-90.
(61) Musso, G.; Bottinelli, E.; Celi, L.; Magnacca, G.; Berlier, G. Influence of surface functionalization on the hydrophilic character of mesoporous silica nanoparticles. *PCCP* **2015**, *17* (21), 13882-13894.

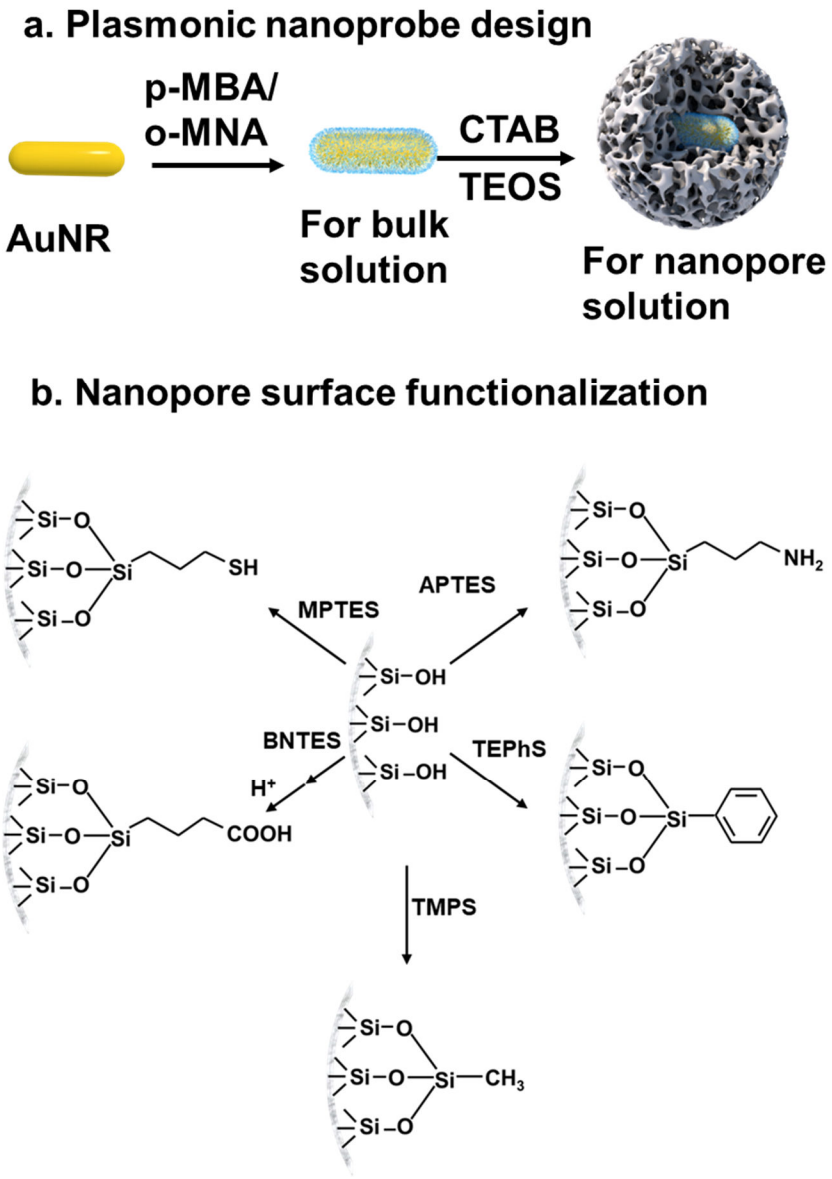

Figure 1. Plasmonic nanosensors for measuring pH and ion concentrations in nanopores and bulk solutions. **a**. Schematic of the synthesis processes for nanosensors for bulk solutions (p-MBA@AuNR and o-MNA@AuNR) and for nanopore solutions ($mSiO_2$@p-MBA@AuNR and $mSiO_2$@o-MNA@AuNR. **b**. Schematic of the design for achieving different functionalizations on the mesoporous silica pore surface.

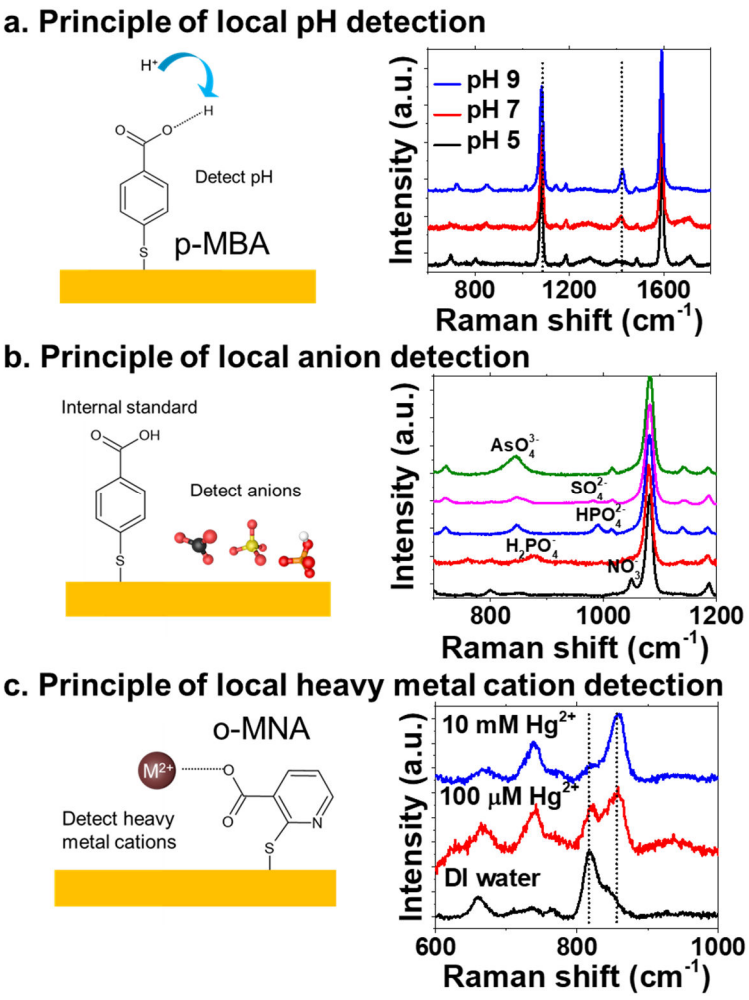

Figure 2. Sensing mechanisms for plasmonic nanosensors. **a**. Principle of local pH detection by SERS. Left: Schematic showing the interaction of the probe molecule (p-MBA) with local protons. Right: Changes in SERS spectra from p-MBA@AuNR at different pH values. Peak intensity at the 1410 cm^{-1} is pH-sensitive (corresponding to COO^- stretching, right dotted line), while peak intensity at 1080 cm^{-1} is pH-insensitive (corresponding to benzene ring breathing and axial deformation, left dotted line). **b**. Principle of local anion detection by SERS. Left: Schematic for using p-MBA as an internal standard to detect anions. Right: SERS spectra from p-MBA@AuNR for 1 M solutions of Na_3AsO_4, Na_2SO_4, Na_2HPO_4, NaH_2PO_4, and $NaNO_3$. **c**. Principle of local cation detection by SERS. Left: Schematic showing the interaction of the probe molecule (o-MNA) with local heavy metal cations. Right: Changes in SERS spectra from o-MNA@AuNR at different Hg^{2+} concentrations. The high ratio between the two Raman peaks at 860 cm^{-1} and 820 cm^{-1} (black dotted line) indicates the high local concentration of mercury.

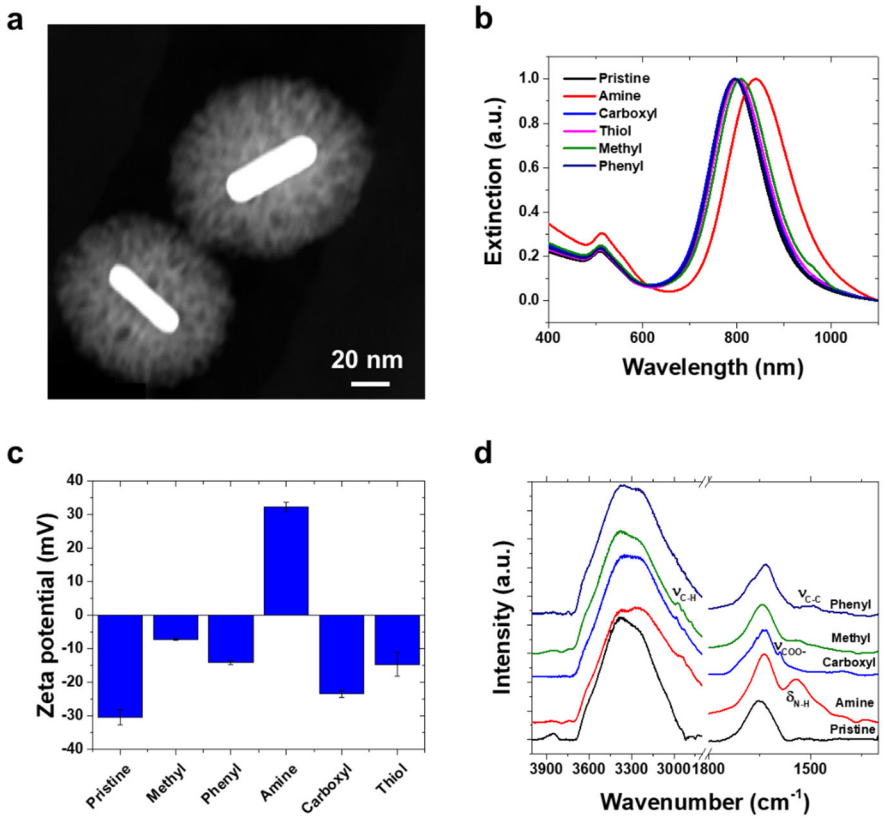

Figure 3. Characterization of plasmonic nanosensors used for measuring ion concentrations in nanopores. **a**. High-angle annular dark-field–scanning electron transmission microscopy images of pristine $mSiO_2$@p-MBA@AuNR. **b.** UV-Vis spectra of pristine and functionalized $mSiO_2$@p-MBA@AuNRs. **c.** Zeta potentials of pristine and functionalized $mSiO_2$@p-MBA@AuNRs. Error bars represent standard errors from measured zeta potentials (obtained from three independent measurements). **d.** FTIR spectra of pristine and functionalized $mSiO_2$@p-MBA@AuNRs.

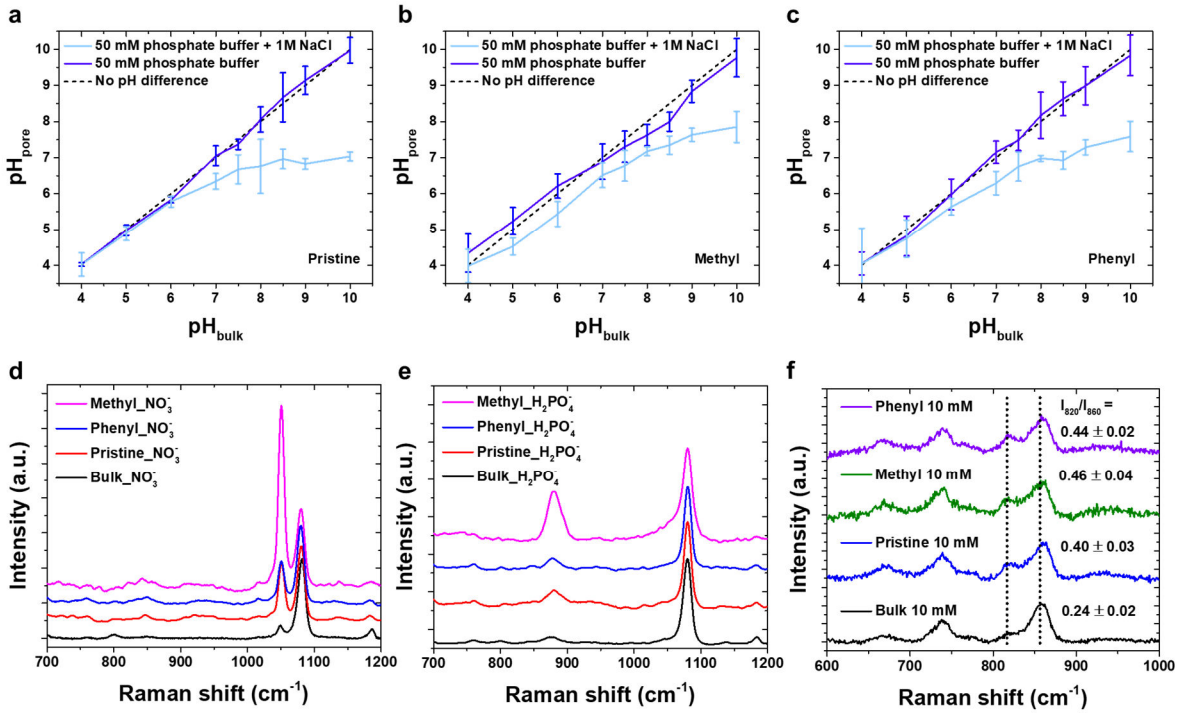

Figure 4. Comparing the pH (**a-c**) and ion concentrations (**d-f**) in pristine and in methyl- and phenyl-functionalized hydrophobic silica nanopores with pH and ion concentrations in bulk solutions. **a-c**. pH behavior in these nanopores exhibited strong dependence on the ionic strengths of buffered bulk solutions: pH_{pore} close to pH_{bulk} at 50 mM phosphate buffer, while pH_{pore} smaller than pH_{bulk} at 50 mM phosphate buffer with 1 M NaCl. Black dashed lines represent the condition where pH_{pore} equals pH_{bulk} in the entire pH range (4–10). Error bars represent standard errors from measured Raman signal intensities (obtained from eight independent measurements). **d-e**.SERS spectra of anions with p-MBA in nanopore and bulk solutions. After the peak intensities were normalized to p-MBA, both nitrate and phosphate exhibited enhanced concentrations in nanopores. The nitrate peak is near 1050 cm^{-1}; the phosphate peak is near 875 cm^{-1}. **f**. SERS spectra show decreased mercury concentration in nanopore solutions compared to the bulk solution. The ratio between the two Raman peaks at 860 cm^{-1} and 820 cm^{-1} (black dotted line) indicates the local concentration of mercury.

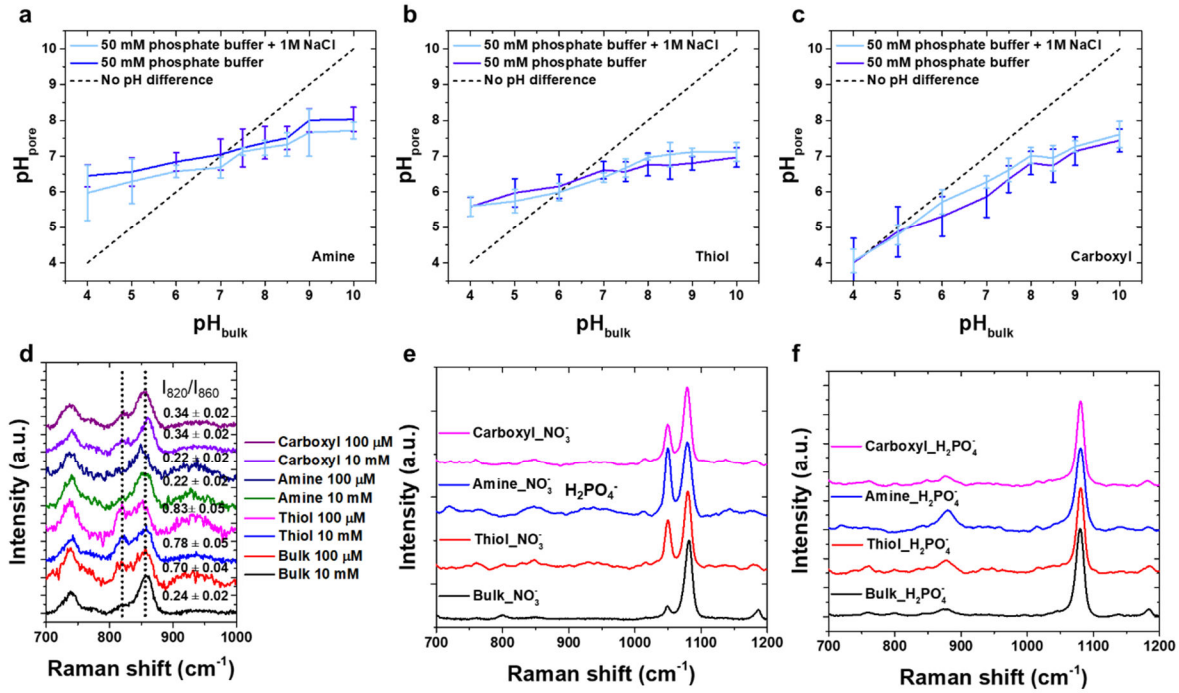

Figure 5. Comparing the pH (**a-c**) and ion concentrations (**d-f**) in amine, thiol, and carboxyl functionalized hydrophilic silica nanopores with the pH and ion concentrations in bulk solutions. **a-c.** pH_{pore} falls into the ranges of 6–8, 5.5–7.5, and 4–7.5 for amine, thiol, and carboxyl functionalized nanopores, respectively. Black dashed lines represent the condition where pH_{pore} equals pH_{bulk} in the entire pH range (4-10). Error bars represent standard errors from measured Raman signal intensities (obtained from eight independent measurements). **d**. SERS spectra show that mercury concentrations in nanopores are dependent on the functional group and independent of the bulk concentrations. The ratio between the intensities of the two Raman peaks at 860 cm^{-1} and 820 cm^{-1} (black dotted line) indicates the local concentration of mercury. **e-f**. SERS spectra of anions with p-MBA in nanopore and bulk solutions. After the peak intensities are normalized to p-MBA, both nitrate and phosphate exhibit enhanced concentrations in nanopores. The nitrate peak is near 1050 cm^{-1}; the phosphate peak is near 875 cm^{-1}.

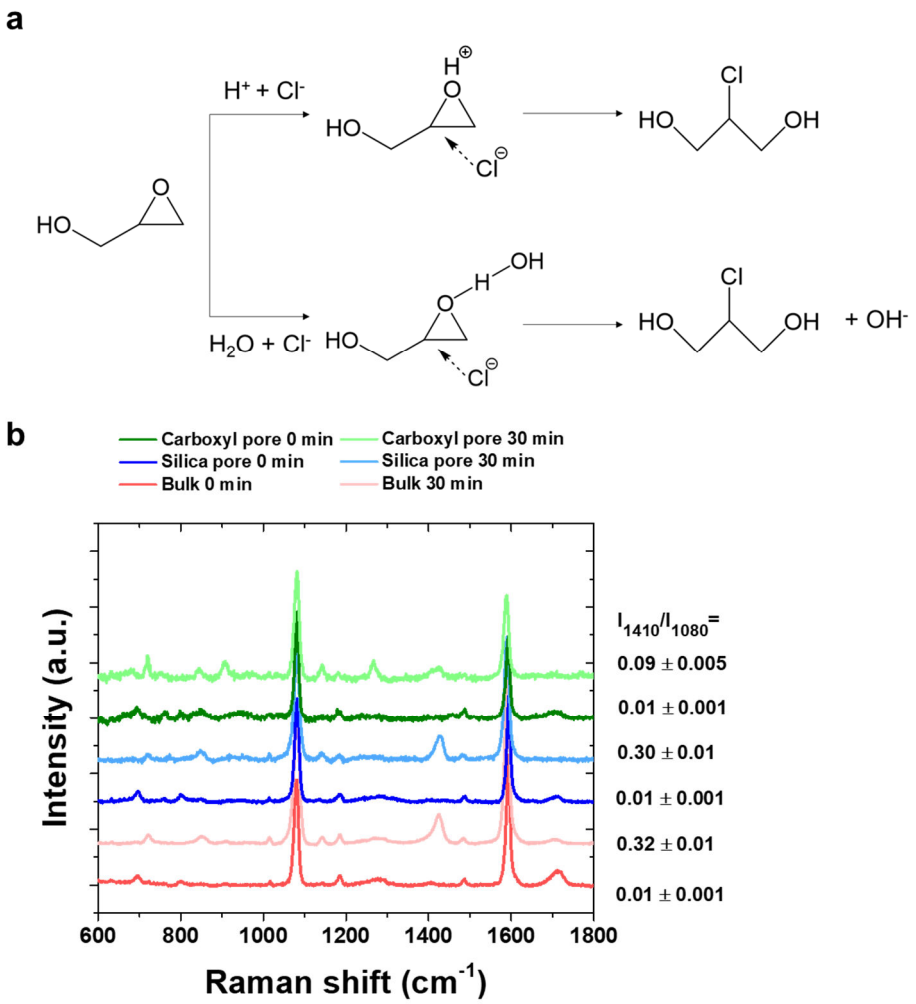

Figure 6. Monitoring the local pH change in carboxyl-functionalized silica nanopores, pristine silica nanopores, and bulk solutions when the glycidol rupture reaction happens. **a**. Schematic of reaction routes for glycidol rupture, which releases OH^- to increase pH. **b**. SERS spectra of carboxyl-functionalized $mSiO_2$@p-MBA@AuNR, pristine $mSiO_2$@p-MBA@AuNR, and p-MBA@AuNR during the glycidol rupture reaction (NaCl 750 mM and glycidol 150 mM, starting pH 3). The SERS spectra are normalized by the peak intensities at 1080 cm^{-1}, which are pH insensitive. The intensities of the peaks at 1410 cm^{-1} increase with increasing local pH. While the local pH in pristine silica nanopores and bulk solutions obviously increases, there is only a minor increase of pH in carboxyl functionalized nanopores.

TOC


Hydrophobic nanopores
Hydrophilic nanopores
Bulk
Enhanced anion and suppressed cation concentrations
Strong ion-functional group interactions